Inorganic Chemistry

Article

pubs.acs.org/IC

Spectroscopic and Computational Studies of a Small-Molecule Functional Mimic of Iron Superoxide Dismutase, Iron 2,6-Diacetylpyridinebis(semioxamazide)

Craig T. Gutman and Thomas C. Brunold*

Department of Chemistry, University of Wisconsin—Madison, Madison, Wisconsin 53706, United States

Supporting Information

ABSTRACT: Iron 2,6-diacetylpyridinebis(semioxamazide) (Fe(dapsox)) is a heptacoordinate pentagonal bipyramidal, functional mimic of iron-dependent superoxide dismutase that has been well-characterized on the basis of kinetics and mechanistic studies; however, prior to our studies, its electronic structure had yet to be examined. This paper details our initial characterization of Fe(dapsox) in both its reduced and oxidized states, by electronic absorption (Abs) and low-temperature magnetic circular dichroism spectroscopies. Density functional theory (DFT) geometry optimizations have yielded models in good agreement with the published crystal structures. Time-dependent DFT and INDO/S-CI calculations performed on these models successfully reproduce the experimental Abs spectra and identify intense, low-energy transitions in the reduced complex ($Fe^{II}(H_2dapsox)$) as metal-to-ligand charge transfer transitions, suggesting the presence of π-backbonding in this complex. This backbonding, along, with the proton uptake accompanying metal ion reduction, provides a compelling mechanism by which the metal-centered redox potential is correctly tuned for catalytic superoxide disproportionation.

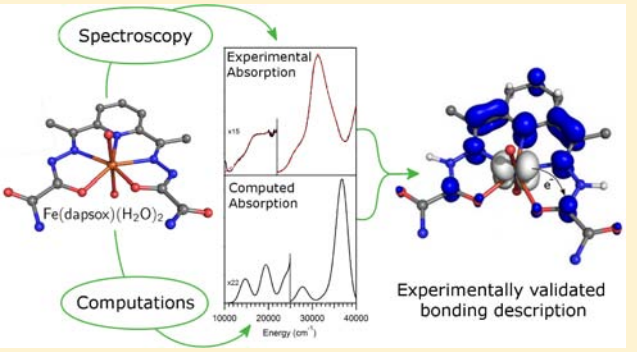

INTRODUCTION

As a result of electron leakage during aerobic metabolism, all aerotolerant organisms must be able to deal with the generation of superoxide ($O_2^{\bullet -}$), a reactive radical anion.[1,2] Superoxide poses a significant threat to a wide variety of biological macromolecules, including DNA, proteins, and cellular lipid bilayers, as a result of its oxidizing power.[1,2] To combat superoxide, nature has evolved a family of enzymes called superoxide dismutases (SODs).[1,3,4] There are several distinct classes of SODs that differ with respect to their metal cofactor; i.e., Cu/Zn-, Fe-, Mn-, and NiSODs.[1,3,4] Despite their different metal cofactors, all SODs catalyze the disproportionation of 2 equiv of superoxide with two protons to O_2 and H_2O_2. This disproportionation occurs with the catalytic metal center cycling between two oxidation states in a classic ping-pong type mechanism (see eqs 1a and 1b).[1,5−7] Consequently, it is necessary that the metal ion's redox potential lie between the reduction potentials for conversion of oxygen to superoxide (−160 mV vs normal hydrogen electrode, NHE) and conversion of superoxide to hydrogen peroxide (890 mV vs NHE).[8]

$$M(ox)SOD + O_2^{\bullet -} + H^+ \rightarrow M(red)SODH^+ + O_2 \quad (1a)$$

$$M(red)SODH^+ + O_2^{\bullet -} + H^+ \rightarrow M(ox)SOD + H_2O_2 \quad (1b)$$

The Fe- and Mn-containing SODs, while unrelated to the Cu/Zn- and NiSODs, are structurally homologous[5,9,10] possessing virtually identical active sites.[11,12] In each case, the metal ion resides in a trigonal bipyramidal ligand environment composed of one aspartate and two histidines in the equatorial plane, and axially a third histidine and a solvent molecule that is OH^- in the oxidized (M^{III}) state and H_2O in the reduced (M^{II}) state.[13]

The importance of SOD is highlighted by the fact that elevated cellular levels of superoxide have been implicated in a variety of diseases and disorders, including several inflammatory disorders, familial amyotrophic lateral sclerosis, Parkinson's disease, and Alzheimer's disease.[14−17] As such, there is a significant interest in the discovery and optimization of synthetic, small-molecule, functional mimics of SODs. Ivanović-Burmazović and co-workers[18,19] have developed a class of functional SOD mimics based on the so-called dapsox ligand [dapsox = 2,6-diacetylpyridinebis(semioxamazide)] (see Figure 1). Dapsox is a rigid acyclic molecule that will ligate to a metal in a roughly planar, pentachelate fashion that, with the additional ligation of two axial molecules, yields a heptacoordinate, pseudopentagonal bipyramidal metal complex.[19] They were able to show, through the use of cyclic voltammetry in dimethyl sulfoxide (DMSO), that dapsox complexes of both Mn and Fe (i) possess the correct $M^{III/II}$ redox potentials for

Received: July 16, 2012
Published: November 9, 2012

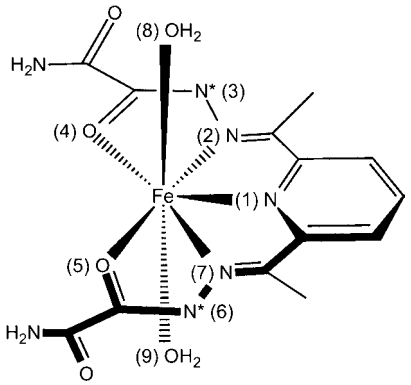

Figure 1. Chemical structure of Fe(dapsox)$(H_2O)_2$. The asterisks show the two sites of protonation upon reduction of the metal center.

$O_2^{\bullet -}$ disproportionation (−180 mV vs NHE for $Fe^{III/II}$and 650 mV vs NHE for $Mn^{III/II}$ and (ii) exhibit catalytic SOD activity.[19] They have also used stop-flow kinetics studies in DMSO and indirect activity assays in aqueous solution to show that both the Mn- and Fe(dapsox) complexes are among some of the more active SOD catalysts, displaying turnover rate constants within an order of magnitude of native MnSOD.[19] However, despite their thorough kinetics and mechanistic characterization, the mechanism by which the metal-centered redox potentials of Fe- and Mn-dapsox are correctly tuned for efficient superoxide dismutation has not yet been thoroughly investigated.

To fill this gap in our understanding, we have characterized both the reduced and oxidized Fe(dapsox) complexes using electronic absorption and magnetic circular dichroism spectroscopies in conjunction with density functional theory (DFT), semiempirical INDO/S-CI, and time-dependent DFT calculations to develop experimentally validated geometric and electronic structure descriptions for these species. On the basis of these results, we propose that a combination of metal−ligand π-backbonding and proton uptake accompanying metal ion reduction serve to properly tune the $Fe^{III/II}$ redox potential for SOD catalysis.

EXPERIMENTAL SECTION

Synthesis, Materials, and Methods. Oxamic hydrazide was obtained from TCI America (Portland, OR), while all other reagents were obtained from Sigma−Aldrich (St. Louis, MO). All reagents were used as received unless otherwise noted.

Fe(dapsox). $[Fe^{III}(dapsox)(H_2O)_2]NO_3$ was synthesized as reported in the literature[19] with the exceptions that the product was recovered via precipitation by addition of excess ether, and that the reaction yielded the oxidized (Fe^{III}) complex and not, as previously reported, the reduced (Fe^{II}) form. The product was then purified via recrystallization by diffusion of Et_2O into a saturated *N*,*N*-dimtheylformamide (DMF) solution of $[Fe^{III}(dapsox)(H_2O)_2]NO_3$. $[Fe^{II}(H_2dapsox)]^{2+}$ was generated by the reduction of an air-free aqueous solution of $[Fe^{III}(dapsox)(H_2O)_2]NO_3$ with excess sodium dithionite under an N_2 atmosphere.

Spectroscopy. *Electronic Absorption and Magnetic Circular Dichroism Data.* Room-temperature electronic absorption (Abs) spectra were obtained on a Varian Cary 5e spectrophotometer, while low-temperature Abs and magnetic circular dichroism (MCD) spectra were collected on a Jasco J-715 spectropolarimeter in conjunction with an Oxford Instruments SM-4000 8 T superconducting magneto-cryostat. The CD signal and glass-strain contributions to the MCD spectra were removed by subtracting the −7 T data from the +7 T data. The samples used in these studies are dissolved in 40:60 (v/v) mixtures of 100 mM NaH_2PO_4 pH 2.0 buffer/glycerol and of 100 mM Na_2HPO_4 pH 7.0 buffer/glycerol for the oxidized and reduced complexes, respectively.

X-band Electron Paramagnetic Resonance Data. The electron paramagnetic resonance (EPR) spectrum of $[Fe^{III}(dapsox)(H_2O)_2]^+$ in 100 mM NaH_2PO_4 buffer, pH 2.0, was collected on a Bruker ESP 300E spectrometer equipped with an Oxford ESR 900 continuous-flow liquid helium cryostat and an Oxford ITC4 temperature controller. The spectrum was obtained at 7.0 K with the following instrument settings: frequency = 9.38 GHz, microwave power = 10.02 mW, gain = 40 dB, modulation amplitude = 10 G, conversion time = 20 ms, time constant = 163.84 ms, range = 0−5000 G, and resolution = 5000 points. EPR spectral simulations were carried out with the EasySpin software package.[20]

Computations. *Geometry Optimizations.* The Amsterdam Density Functional (ADF) software package was used to perform spin-unrestricted density functional theory (DFT) geometry optimizations[21−24] for both reduced and oxidized Fe(dapsox). In each case, the initial geometry was taken from the published[18] crystal structure of the oxidized complex, as deposited in the Cambridge Structural Database (structure code WUTPIK), with the appropriate protons being added for the reduced complex (see Results section). For both complexes, optimizations in all viable spin states were performed; that is, $S = {}^5/_2$, ${}^3/_2$, and ${}^1/_2$ for the Fe^{III} bound species and S = 2, 1, and 0 for the Fe^{II} bound species. All atoms were modeled by use of triple-ζ Slater-type orbitals with a single set of polarization functions (basis set IV). An integration constant of 4.0 and the Vosko−Wilk−Nusair[25] local density approximation were employed, along with the nonlocal gradient corrections of Becke[26] and Perdew.[27] The core orbitals were frozen through 1s (C, N, and O) or 2p (Fe).

Single-Point Calculations. The ORCA 2.8 software package developed by Dr. Frank Neese[28] was used to perform single-point DFT calculations on the geometry-optimized models of the reduced and oxidized Fe(dapsox) complexes in their S = 2 and $S = {}^5/_2$ spin ground states, respectively. These models were oriented in space according to their calculated **D**-tensor (vide infra) prior to the single-point computations. Becke's three-parameter hybrid functional for exchange[26,29] and the Lee−Yang−Parr functional for correlation (B3LYP)[30] were used with the polarized-split-valence SV(P) basis set[31] and the SV/C auxiliary basis set[32] for all atoms except for the Fe ion and the ligating nitrogen and oxygen atoms, for which Ahlrich's polarized triple-ζ-valence (TZVP) basis set[33] with one polarization function was employed. All computations were performed as spin-unrestricted, with an integration grid of size 4 (302 Lebedev points). Isosurface plots of the molecular orbitals (MOs) were generated by use of the PyMol program with an isodensity value of 0.05 au.[34]

Electron Paramagnetic Resonance Calculations. The EPR parameters were calculated with the ORCA 2.9.1 software package[35] by use of the geometry-optimized models of the reduced and oxidized Fe(dapsox) complexes in their S = 2 and $S = {}^5/_2$ spin ground states, respectively. As for the single-point calculations, Becke's three-parameter hybrid functional for exchange[26,29] and the Lee−Yang−Parr functional for correlation (B3LYP)[30] were used. For the Fe ion, the "core properties" with triple polarization basis set[36,37] was used, while the IGLO-III basis set[38] was used for the ligating nitrogen and oxygen atoms. For all other atoms the SV(P) basis set[31] was used. The resolution of the identity (RI) approximation was used to speed up the calculation of the Coulomb term by approximating the molecule's charge distribution with the SV/J auxiliary basis set. The EPR **g** and **D** tensors were computed by use of coupled-perturbed self-consistent field theory[39] with a complete mean-field treatment of spin-orbit coupling and an origin defined by the center of electronic charge.[40]

Time-Dependent Density Functional Theory. All time-dependent density functional theory (TD-DFT) calculations were performed with the ORCA 2.8 software package[28] within the Tamm−Dancoff approximation[41,42] and using the functional, basis sets, and model geometries specified above for the single-point calculations. A total of 50 excited states were constructed from all molecular orbitals (MOs) within ±3 hartree of the highest occupied molecular orbital (HOMO)/lowest unoccupied molecular orbital (LUMO) energy gap. The TD-DFT results were used to simulate Abs spectra with the

dx.doi.org/10.1021/ic301547z | Inorg. Chem. 2012, 51, 12729−12737

assumption that each electronic transition gives rise to a Gaussian band with a full width at half-maximum of 2750 cm^{-1}, a value that was chosen on the basis of our spectral analysis of the experimental data. The natures of key electronic transitions were explored on the basis of electron density difference maps (EDDMs), which were generated by use of the PyMol program with an isodensity value of 0.003 au.[34]

Semiempirical Intermediate Neglect of Differential Overlap/Spectroscopic Parametrization with Configuration Interaction. Semiempirical intermediate neglect of differential overlap/spectroscopic parametrization with configuration interaction (INDO/S-CI) calculations were carried out with the ORCA 2.8 software package[28] for the $S = {}^5/_2$ and $S = 2$ DFT geometry-optimized models of $[Fe^{III}(dapsox)(H_2O)_2]^+$ and $[Fe^{II}(H_2dapsox)(H_2O)_2]^{2+}$, respectively. This program uses the model of Ridley and Zerner[43] and Zerner et al.,[44] the valence shell ionization potentials and Slater–Condon parameters listed by Bacon and Zerner,[45] and the standard interaction factors $f_{p\sigma p\sigma} = 1.267$ and $f_{p\pi p\pi} = 0.585$. Spin-unrestricted Hartree–Fock self-consistent-field calculations were tightly converged on the $S = {}^5/_2$ and $S = 2$ ground states of the oxidized and reduced complexes, respectively. These then served as the reference states for configuration interaction calculations. Calculations of electronic transition energies and intensities considered all possible single excitations among MOs within ±3 eV of the HOMOs. The INDO/S results were used to simulate Abs spectra assuming that each electronic transition gives rise to a Gaussian band with a full width at half-maximum of 2750 cm^{-1}, and EDDMs were generated by use of the PyMol program[34] with an isodensity value of 0.003 au, as for the TD-DFT results.

RESULTS

Experimental Studies. *Ligand Protonation State.* The dapsox ligand contains two basic nitrogens (see Figure 1); hence, the ligand's protonation state is variable. When the Fe^{III} complex is synthesized with the weakly coordinating perchlorate counterion, the dapsox ligand is known to be doubly deprotonated.[18] With the nitrate counterion, the resulting solvated complex is spectroscopically identical to the perchlorate salt (Supporting Information, Figure S1), strongly suggesting that it can be formulated as $[Fe^{III}(dapsox)(H_2O)_2]NO_3$, also featuring a doubly deprotonated dapsox ligand. Alternatively, in the Fe^{II}-bound form, the ligand has been shown crystallographically[19] to be doubly protonated, yielding $[Fe^{II}(H_2dapsox)]^{2+}$.

Electronic Absorption and Magnetic Circular Dichroic Spectra. As expected for complexes whose ligands contain extensive π-conjugation, the Abs and MCD spectra of the reduced and oxidized Fe(dapsox) complexes show multiple high-intensity features in the UV region; however, both sets of spectra also exhibit weaker, but clearly discernible, features in the visible region. In the case of the oxidized $[Fe^{III}(dapsox)(H_2O)_2]^+$ complex, a broad shoulder centered at 31 500 cm^{-1} ($\varepsilon \approx 6500$ $M^{-1}\cdot cm^{-1}$) and a more intense feature peaking at >40 000 cm^{-1} ($\varepsilon \geq 9000$ $M^{-1}\cdot cm^{-1}$) are discernible in the Abs spectrum (Figure 2, top). In the corresponding MCD spectrum (Figure 2, bottom), four broad bands with alternating signs are observed at ∼18 500, 23 200, 31 000, and 37 000 cm^{-1}. The intensities of these bands are temperature-dependent (Supporting Information, Figure S2), indicating that the corresponding transitions gain intensity via a C-term mechanism, consistent with a paramagnetic species. To resolve the individual transitions contributing to the Abs and MCD spectra, these spectra were iteratively fit with the minimum acceptable number of Gaussian bands of constant width. Good agreement between the experimental and simulated spectra over the entire 11 000–40 000 cm^{-1} range was achieved with 12 Gaussian bands (Figure 2 and Table 1).

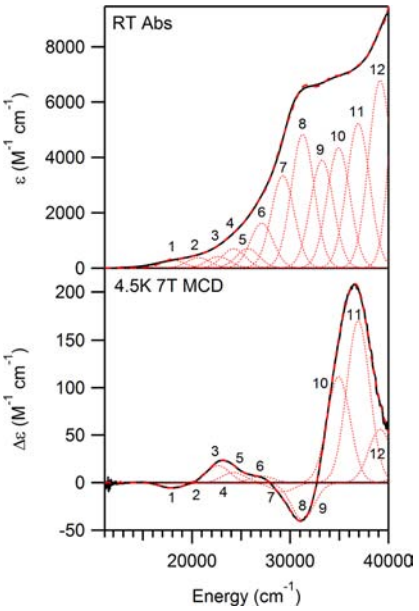

Figure 2. Room-temperature Abs (top) and 4.5 K, 7 T MCD (bottom) spectra of $[Fe^{III}(dapsox)(H_2O)_2]^+$ (thick black lines). Individual Gaussian bands are shown as thin dotted red lines, and the simulated spectra are shown as thick dashed red lines.

Table 1. Spectral Parameters from Iterative Fits of Abs and MCD Data of $[Fe^{III}(dapsox)(H_2O)_2]^+$

band	E (cm^{-1})	ε ($M^{-1}\cdot cm^{-1}$)	$\Delta\varepsilon$ ($M^{-1}\cdot cm^{-1}$)	C/D ratio
1	18 010	291	−5.6	0.019
2	20 675	374	0.02	4.05×10^{-5}
3	22 677	412	17.9	0.043
4	24 235	689	10.7	0.015
5	25 691	692	0.1	9.16×10^{-5}
6	27 095	1615	6.9	0.004
7	29 243	3335	−9.7	0.003
8	31 275	4824	−38.9	0.008
9	33 233	3899	0.5	1.24×10^{-4}
10	34 921	4341	111.4	0.026
11	36 924	5221	170.1	0.033
12	39 158	6771	55.9	0.008

The Abs spectrum of the reduced $[Fe^{II}(H_2dapsox)(H_2O)_2]^{2+}$ complex (Figure 3, top) displays a broad feature centered at 33 000 cm^{-1} ($\varepsilon \approx 29\,000$ $M^{-1}\cdot cm^{-1}$) with a shoulder centered at ∼26 500 cm^{-1} ($\varepsilon \approx 5000$ $M^{-1}\cdot cm^{-1}$) and a weaker feature located at ∼17 000 cm^{-1} ($\varepsilon \approx 600$ $M^{-1}\cdot cm^{-1}$) with a shoulder at ∼13 000 cm^{-1} ($\varepsilon \approx 200$ $M^{-1}\cdot cm^{-1}$). The corresponding MCD spectrum (Figure 3, bottom) exhibits three positively signed bands centered at ∼14 250, 28 200, and and 32 100 cm^{-1} and two negative features located at 18 000 and 39 000 cm^{-1}. All of these features show temperature-dependent intensity (Supporting Information, Figure S3), indicating that they also gain intensity via a C-term mechanism and thus derive from a paramagnetic species. Iterative fitting of the Abs and MCD spectra with the minimum acceptable number of Gaussian bands of constant width was used to resolve the individual electronic transitions. Good agreement between the experimental and simulated spectra over the entire 10 000–40 000 cm^{-1} region was achieved with 14 Gaussian bands (Figure 3 and Table 2).

dx.doi.org/10.1021/ic301547z | Inorg. Chem. 2012, 51, 12729–12737

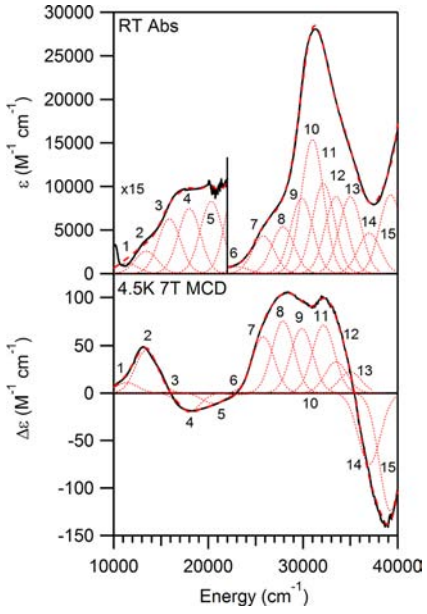

Figure 3. Room-temperature Abs (top) and 4.5 K, 7 T MCD (bottom) spectra of $[Fe^{II}(H_2dapsox)(H_2O)_2]^{2+}$ (thick black lines). Individual Gaussian bands are shown as thin dotted red lines, and the simulated spectra are shown as thick dashed red lines.

Table 2. Spectral Parameters from Iterative Fits of Abs and MCD Data of $[Fe^{II}(H_2dapsox)(H_2O_2)]^{2+}$

band	E (cm^{-1})	ε ($M^{-1}\cdot cm^{-1}$)	$\Delta\varepsilon$ ($M^{-1}\cdot cm^{-1}$)	C/D ratio
1	11 386	78	10.8	0.138
2	13 450	170	44.9	0.264
3	15 877	417	0.90	0.002
4	17 996	497	−19.2	0.039
5	20 511	552	−10.9	0.020
6	23 049	759	−1.94	0.003
7	25 805	4303	59.0	0.014
8	27 892	5360	75.5	0.014
9	29 870	8633	67.7	0.008
10	31 000	15 392	−0.52	3.40×10^{-5}
11	32 160	10 307	71.1	0.007
12	33 500	8833	32.7	0.004
13	35 000	8812	22.0	0.003
14	39 250	9025	−124	0.014

Electron Paramagnetic Resonance Spectrum. The X-band EPR spectrum of $[Fe^{III}(dapsox)(H_2O)_2]^+$ at 7.0 K exhibits two broad features roughly centered at $g_{eff} \approx 5.69$ and 1.92 (Supporting Information, Figure S4). This spectrum was simulated reasonably well by use of the spin Hamiltonian for an $S = {}^5/_2$ species[20] and the parameters in Table 3, where **D** and **E** are the axial and rhombic zero-field splitting tensors, respectively.

Computational Studies. *Geometry Optimizations.* To aid in the interpretation of the spectroscopic data and to obtain a quantitative bonding description for Fe(dapsox), electronic structure calculations were performed for both the reduced and oxidized complexes. The models were constructed by using the X-ray crystal structure[18] of oxidized $[Fe^{III}(dapsox)(H_2O)_2]ClO_4$ (CSD code WUTPIK) as the starting point for geometry optimization calculations (see Experimental Section). For both complexes, the high-spin state ($S = {}^5/_2$ and 2 for the oxidized and reduced complexes, respectively) was found to be the most stable spin configuration (Supporting Information, Table S1). As shown in Table 4, the optimized models reproduce the X-ray crystallographic structures quite well. In the case of the oxidized model, all of the computed Fe^{III}–N/O(dapsox) bond lengths deviate from the crystal structure values[18] by less than 0.06 Å. Although the Fe^{III}–OH_2 bond lengths for the axially bound water ligands are overestimated by up to 0.18 Å, this discrepancy between the experimental and computational bond distances can be attributed, at least in part, to intermolecular interactions within the crystal. Most importantly, in the solid state both axial water ligands interact with hydrogen-bond acceptors (a water molecule and a dapsox carbonyl oxygen in the next unit cell at O···O distances of 2.61 and 2.93 Å from the upper and lower axial ligands, respectively), which causes these ligands to acquire a substantial degree of hydroxide character and, thus, to move closer to the Fe^{III} center.

Table 3. Experimental and Computed EPR Parameters for $[Fe^{III}(dapsox)(H_2O)_2]^+$

parameter	experimental fit	computed
g_1	2.057	2.009
g_2	1.951	2.0117
g_3	1.942	2.0122
D (cm^{-1})	−1.08	−0.463
E/D	0.075	0.109

Table 4. Bond Lengths and Bond Angles for $[Fe(dapsox)(H_2O)_2]^{2+/+}$ as Obtained by X-ray Crystallography and DFT Geometry Optimizations

	Fe^{III} Xtal structure[a]	Fe^{III} optimized	Fe^{II} Xtal structure[b]	Fe^{II} optimized
	Bond Lengths (Å)			
Fe–N1 (pyridine)	2.195	2.198	2.205	2.234
Fe–N2	2.202	2.204	2.233	2.238
Fe–N7	2.195	2.202	2.218	2.215
Fe–O4 (carbonyl)	2.066	2.105	2.179	2.224
Fe–O5 (carbonyl)	2.046	2.103	2.195	2.219
Fe–O8 (water)	2.038	2.203	2.159	2.232
Fe–O9 (water)	2.019	2.202	2.145	2.221
	Bond Angles (deg)			
α(O8–Fe–O9)	178	175	166	175
α(O5–Fe–N7)	71.9	71.4	71.8	72.6
α(N7–Fe–N1)	70.1	70.6	70.2	69.8
α(N1–Fe–N2)	69.8	70.5	69.8	69.4
α(N2–Fe–O4)	71.1	71.4	71.1	72.1

[a]Reference 18; CSD code WUTPIK.. [b]Reference 19; CSD code TIRFAC.

In the case of the reduced complex, good agreement is again observed between the DFT-optimized and experimental structures[19] (CSD code TIRFAC), with the computed Fe^{II}–N/O(dapsox) bond lengths deviating by less than 0.05 Å from the X-ray crystallographic data. The optimized Fe^{II}–OH_2 bond lengths also agree well with the experimental values, with bond lengths elongated by only 0.07 and 0.08 Å for Fe^{II}–O8 and Fe^{II}–O9, respectively.

Calculated Electron Paramagnetic Resonance Parameters and D-Tensor Orientation. A comparison of the experimental and computed EPR parameters for $[Fe^{III}(dapsox)(H_2O)_2]^+$ reveals good agreement between the two sets of parameters (Table 3). In particular, the computational results successfully reproduce the negative sign and magnitude of the axial zero-

dx.doi.org/10.1021/ic301547z | Inorg. Chem. 2012, 51, 12729–12737

field splitting parameter (D) as well as the degree of rhombicity (E/D ratio). Consequently, it is appropriate to use the calculated **D**-tensor orientations to identify the molecular coordinate systems of $[Fe^{III}(dapsox)(H_2O)_2]^+$ and $[Fe^{II}(H_2dapsox)(H_2O)_2]^{2+}$. In both models, the z axis lies approximately along the Fe−pyridine bond vector, the x axis is rotated ∼20° away from the Fe−N2 bond vector, and the y axis lies roughly along the Fe−water bond vectors (Figures 4 and 5).

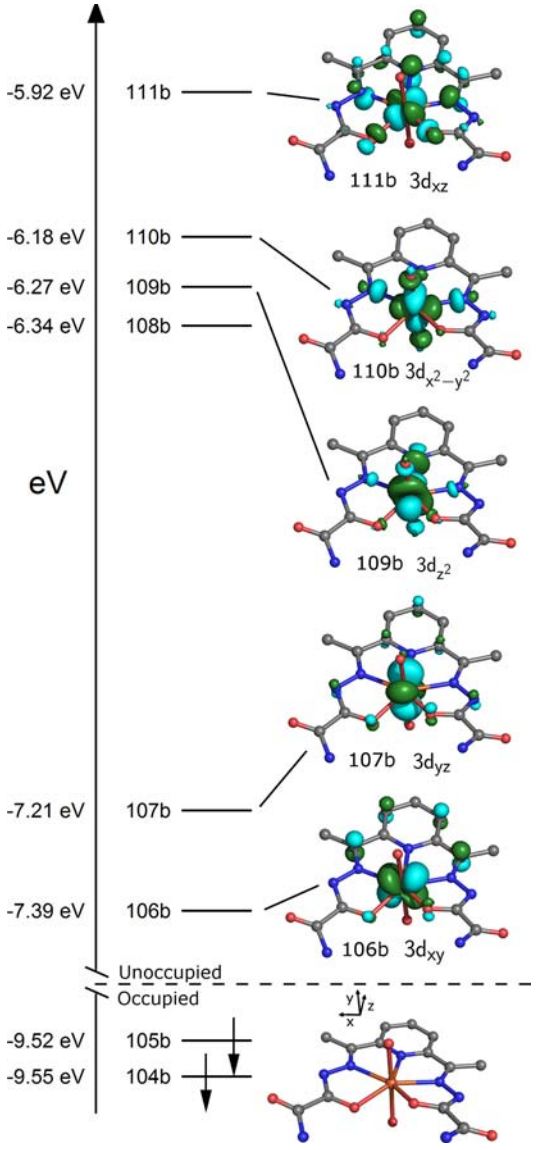

Figure 4. Energy-level diagram of the frontier spin-down MOs, as obtained from a spin-unrestricted DFT calculation on the geometry-optimized $[Fe^{III}(dapsox)(H_2O)_2]^+$ model. Isosurface plots of the unoccupied Fe 3d-based MOs and the molecular coordinate system are shown on the right.

Calculated Molecular Orbital Diagrams. Prompted by the good overall agreement between the experimental and DFT-optimized structures of the Fe(dapsox) complexes, spin-unrestricted DFT calculations were carried out to compute the MO energies and compositions for the oxidized and reduced species. Due to their reduced exchange stabilization, the Fe 3d-based spin-down MOs are higher in energy relative

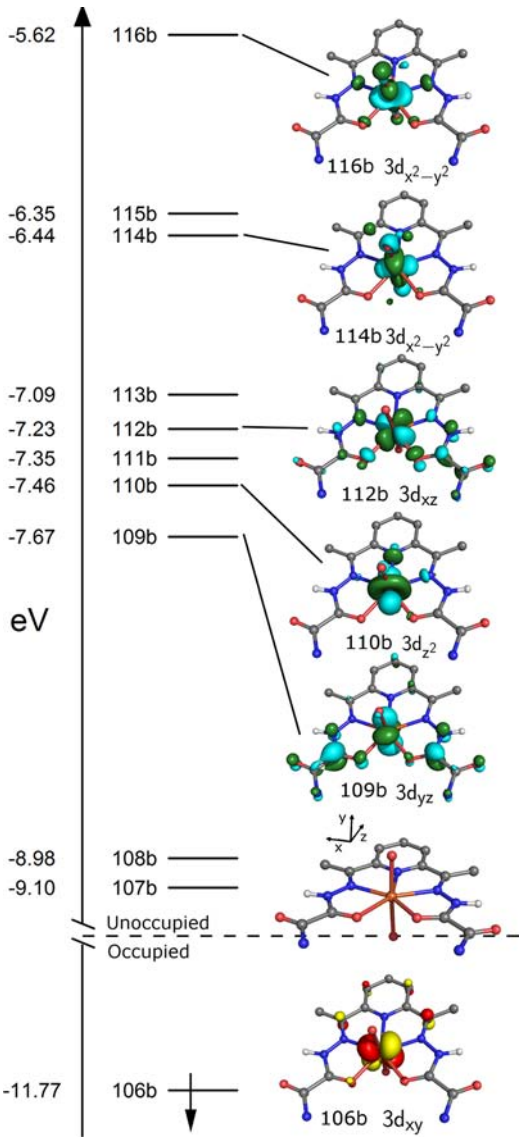

Figure 5. Energy-level diagram of the frontier spin-down MOs, as obtained from a spin-unrestricted DFT calculation on the geometry-optimized $[Fe^{II}(H_2dapsox)(H_2O)_2]^{2+}$ model. Isosurface plots of the Fe 3d-based MOs and the orientation of the molecular coordinate system are shown on the right.

to their spin-up counterparts[47] and, consequently, less strongly mixed with the ligand frontier orbitals. Therefore, for ease of analysis, only the spin-down MOs are discussed here [see Tables 5 and 6 for oxidized and reduced Fe(dapsox), respectively].

In the oxidized model, the splitting pattern of the unoccupied Fe 3d-based spin-down MOs is similar to that expected for a complex with D_{5h} symmetry. However, because in the model the z axis is not aligned with the axial ligand bond vectors, the MO labels differ from those in an ideal pentagonal bipyramidal system. Lowest in energy are the Fe $3d_{xy}$ and $3d_{yz}$ MOs (106b and 107b, respectively), followed by the $3d_{z^2}$ (109b) and $3d_{x^2-y^2}$ (110b) MOs at ∼1 eV higher in energy, and finally, the $3d_{xz}$ MO (111b), which is destabilized by another ∼0.3 eV (Figure 4). This splitting pattern reflects the different types of bonding interactions involving the Fe 3d orbitals and ligand frontier MOs. The Fe $3d_{xy}$ and $3d_{yz}$ orbitals engage in π-type interactions with both the dapsox and water ligands; hence,

dx.doi.org/10.1021/ic301547z | Inorg. Chem. 2012, 51, 12729−12737

Table 5. Energies and Percent Compositions of the Relevant Spin-Down MOs[a] of the Geometry-Optimized $[Fe^{III}(dapsox)(H_2O)_2]^+$ Model

				Fe 3d orbitals (%)					
MO	E (eV)	main contributor	occ	xz	z^2	xy	x^2-y^2	yz	ligand[b] (%)
111b	−5.9199	Fe $3d_{xz}$	0	46.8	0.0	0.0	0.0	3.2	49.3
110b	−6.1792	Fe $3d_{x^2-y^2}$	0	0.0	9.6	3.0	60.3	0.0	26.4
109b	−6.2668	Fe $3d_{z^2}$	0	0.0	64.1	0.7	14.3	0.1	20.3
108b	−6.3379	dapsox	0	26.2	0.1	0.0	0.0	6.5	66.1
107b	−7.2090	Fe $3d_{yz}$	0	0.0	0.1	0.0	0.0	80.6	18.7
106b	−7.3999	Fe $3d_{xy}$	0	0.1	1.3	71.9	1.3	0.0	25.3

[a]As obtained from a spin-unrestricted DFT calculation. [b]Includes contributions from both the dapsox and H_2O ligands.

Table 6. Energies and Percent Compositions of the Relevant Spin-Down MOs[a] of the Geometry-Optimized $[Fe^{II}(H_2dapsox)(H_2O)_2]^{2+}$ Model

				Fe 3d orbitals (%)					
MO	E (eV)	main contributor	occ	xz	x^2-y^2	yz	z^2	xy	ligand[b](%)
116b	−5.6239	Fe $3d_{x^2-y^2}$	0	0.0	41.5	0.2	1.7	0.0	43.7
115b	−6.3544	H_2dapsox	0	0.0	0.2	0.5	0.0	0.0	98.8
114b	−6.4355	Fe $3d_{x^2-y^2}$	0	0.0	46.4	0.0	0.8	0.0	42.3
113b	−7.0879	H_2dapsox	0	0.7	0.0	35.8	1.5	0.0	62.0
112b	−7.2329	Fe $3d_{xz}$	0	64.7	0.0	1.7	0.1	0.1	33.4
111b	−7.3486	H_2dapsox	0	21.1	0.0	0.5	1.5	0.0	76.9
110b	−7.4606	Fe $3d_{z^2}$	0	0.5	0.0	0.9	81.8	0.0	16.8
109b	−7.6705	Fe $3d_{yz}$	0	0.2	0.0	52.6	0.1	0.0	47.1
108b	−8.9766	H_2dapsox	0	0.0	0.0	0.7	0.0	3.6	95.7
107b	−9.0986	H_2dapsox	0	0.0	0.0	3.6	0.0	0.1	94.8
106b	−11.7707	Fe $3d_{xy}$	1	0.1	0.0	0.0	0.0	83.1	16.8

[a]As obtained from a spin-unrestricted DFT calculation. [b]Includes contributions from both the dapsox and H_2O ligands

the antibonding MOs that are primarily based on these orbitals (MOs 106b and 107b) are the least destabilized (lowest in energy) of the Fe 3d-based MOs. Alternatively, the Fe $3d_{z^2}$, $3d_{x^2-y^2}$, and $3d_{xz}$ orbitals all interact with the ligands in σ-type fashions, such that the antibonding MOs derived from these orbitals (MOs 109b−111b) are more strongly destabilized (higher in energy). The energetic ordering of these three MOs can be explained by the fact that the $3d_{z^2}$ and $3d_{x^2-y^2}$ orbitals have significant overlap with the ligand orbitals along only one or two bond vectors, while the $3d_{xz}$ orbital has considerable orbital overlap along four bond vectors.

In the reduced complex, the splitting pattern of the Fe 3d-based spin-down MOs is similar to that of the oxidized complex (Figure 5). One difference, however, is that the $3d_{xy}$ MO (106b) is now occupied and at a much lower energy (relative to the other Fe 3d-based MOs) than in the oxidized complex. Second, due to the protonation of the dapsox ligand (vide supra), the unoccupied MOs with predominant ligand orbital character are stabilized, shifting close in energy to the Fe 3d-based MOs. Finally, two MOs exhibit significant Fe $3d_{x^2-y^2}$ character (114b and 116b), and these MOs are higher in energy than the Fe $3d_{xz}$ MO due to strong metal−ligand σ-antibonding interactions.

Calculated Electronic Absorption Spectra. TD-DFT computations were performed to predict the electronic transition energies and intensities for both the oxidized and reduced complexes. For the oxidized complex, the TD-DFT calculation failed to predict a reasonable Abs spectrum (Supporting Information, Figure S5). This is not unexpected, given that TD-DFT often fails to predict reasonable excitation energies for high-spin ($S = {}^5/_2$) Fe^{III} species.[48] Owing to this failure of the TD-DFT method, semiempirical INDO/S-CI calculations were performed to analyze the Abs spectrum for the oxidized complex. As shown in Figure 6, the results from

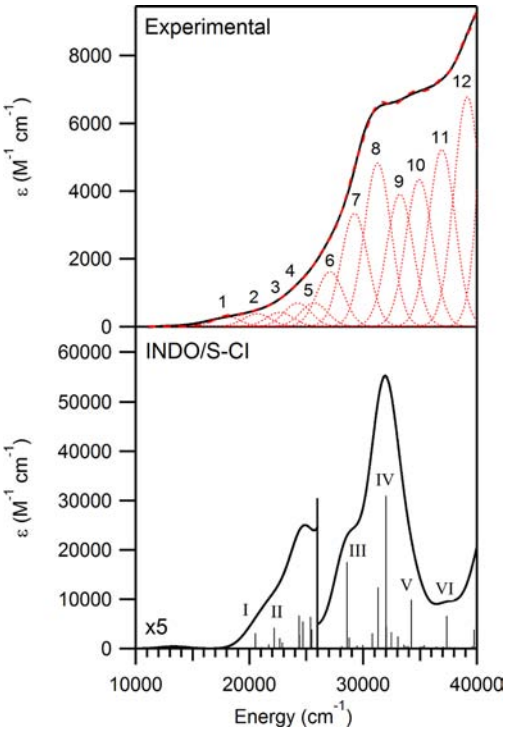

Figure 6. Experimental (top) and INDO/S-CI computed (bottom) Abs spectra of $[Fe^{III}(dapsox)(H_2O)_2]^+$.

dx.doi.org/10.1021/ic301547z | Inorg. Chem. 2012, 51, 12729−12737

this calculation agree quite well with the experimental data. Electron density difference maps (EDDMs) provide visual representations of how the electron density changes between the ground and excited states upon different electronic excitations. By examining the EDDM corresponding to a specific electronic transition, one can determine what type of excitation is occurring (e.g., ligand field, metal-to-ligand charge transfer, ligand-to-metal charge transfer). The EDDMs for the computed transitions (identified by Roman numerals) corresponding to the experimental bands 1 (I), 2 (II), 6 (III), 8 (IV), 10 (V), and 11 (VI) show (Figure 8), as expected, that the lower energy bands in the experimental spectrum arise from transitions that are mainly ligand-to-metal charge transfer (LMCT) in nature, while the higher-energy bands are due to transitions that involve ligand $\pi \rightarrow \pi^*$ excitations.

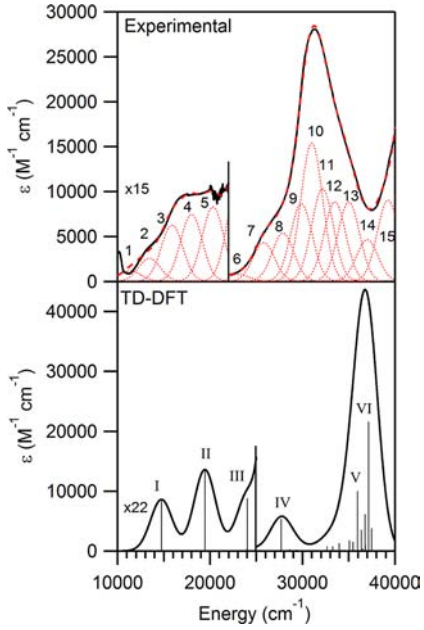

Figure 7. Experimental (top) and TD-DFT computed (bottom) Abs spectra of $[Fe^{III}(dapsox)(H_2O)_2]^{2+}$.

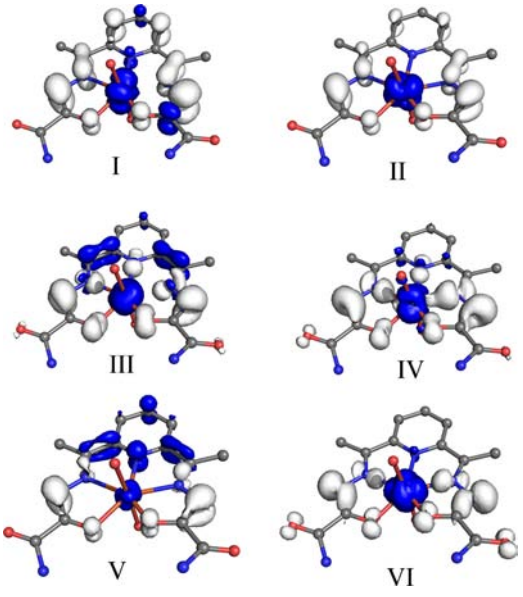

Figure 8. EDDMs for selected INDO/S-CI calculated electronic transitions in $[Fe^{III}(dapsox)(H_2O)_2]^{+}$. White and blue represent electron loss and gain, respectively.

Unlike for the oxidized complex, the TD-DFT calculation for the reduced complex predicts an Abs spectrum that reproduces the experimental spectrum reasonably well (Figure 7), and thus provides an excellent basis for assigning the experimentally observed Abs and MCD features. Examination of the computed spectrum reveals three weak transitions (I, II, and III) present in the low-energy region and three intense transitions (IV, V, and VI) in the high-energy region. The transitions contributing to the lower-energy bands in the predicted Abs spectrum (corresponding to bands 1−5 in the experimental data) are metal-to-ligand charge transfer (MLCT) excitations, as revealed by their EDDMs (Figure 9). As for the oxidized complex, the higher-energy Abs features of the reduced complex are due to transitions that are mostly ligand $\pi \rightarrow \pi^*$ in character (Figure 9). To complement these TD-DFT studies, INDO/S-CI calculations were also performed for the reduced complex. The results from these computations are consistent with those obtained by TD-DFT and also agree quite well with the experimental data (Supporting Information, Figure S6), further validating the use of the INDO/S-CI computational method for the oxidized complex.

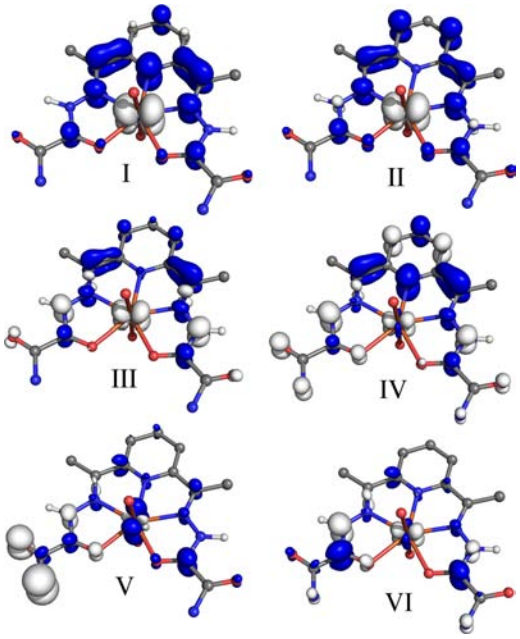

Figure 9. EDDMs for selected TD-DFT calculated electronic transitions for $[Fe^{II}(H_2dapsox)(H_2O)_2]^{2+}$. White and blue represent electron loss and gain, respectively.

DISCUSSION

Geometry Optimization. As expected, the DFT-optimized, average metal−ligand bond length decreases upon oxidation of $Fe^{II}(H_2dapsox)$, from 2.226 to 2.174 Å. This shortening of the bonds reflects both the increased effective nuclear charge of the oxidized metal center, which causes a stabilization of the Fe 3d orbitals, and the destabilization of the ligand frontier orbitals in response to the deprotonation of N2 and N7 of the ligand. This stabilization of the Fe 3d orbitals and destabilization of the ligand frontier orbitals leads to a

dx.doi.org/10.1021/ic301547z | Inorg. Chem. 2012, 51, 12729−12737

better energetic match between them and, thus, stronger metal−ligand bonds.

Tuning of $Fe^{III/II}$ Redox Potential by the Dapsox Ligand. A puzzling feature of the experimental absorption and MCD spectra of the reduced complex is the appearance of bands in the visible/near-IR spectral region. On the basis of their large **C**/**D** ratios, relative to the higher-energy features, one would be tempted to assign them as Fe^{II} d → d transitions; however, their energies of 11 386 and 13 450 cm^{-1} are much higher than expected for Fe^{II} complexes.[49] The results of our computations show (Figure 9) that the low-energy transitions at 14 300 cm^{-1} (transition I) and 18 700 cm^{-1} (transition II) are in fact due to MLCT transitions rather than Fe^{II} d → d transitions, which TD-DFT predicts to occur at ∼8300 cm^{-1} in this complex. The presence of MLCT transitions at relatively low energies in the reduced complex is in contrast to what is found for the oxidized complex, where the lower-energy transitions are composed mostly of LMCT excitations (Figure 8). The nature of these low-energy transitions can help provide insight into the mechanism by which the $Fe^{III/II}$ midpoint potential is tuned by the dapsox ligand, such that the complex is able to catalyze both the reduction and oxidation of superoxide (recall that for $Fe(H_2O)_6$, $E°$ = 771 mV vs NHE[50] and that the ideal potential for SOD activity is ∼360 mV).[8]

In FeSOD, metal-ion reduction is coupled to proton uptake, and as such, both the electron transfer (ε_{ET}) and proton transfer (ε_{PT}) energies contribute to the $E°$ of the metal ion.[51] In previous work,[51] we have shown that in FeSOD, the fine-tuning of $E°$ is accomplished by modulating ε_{PT} rather than ε_{ET}. This modulation of ε_{PT} is largely controlled by the positioning of a second-sphere glutamine residue (Gln69 in FeSOD from *Escherichia coli*) within the protein matrix.[51,52] This glutamine is positioned close to the active site and forms a strong hydrogen bond with the coordinated solvent. As an obligate H-bond donor, the Gln residue stabilizes Fe^{III}-bound OH^- over Fe^{II}-bound H_2O and in effect serves to lower $E°$ of the enzyme. This additional stabilization is important because, as a whole, the first coordination sphere of the enzyme is not a strong enough electron donor to sufficiently stabilize the Fe^{III} state of the enzyme for optimal SOD activity.[51]

In contrast to FeSOD, the dianionic dapsox ligand is a strong electron donor, and as such, it likely stabilizes the Fe^{III} state over the Fe^{II} state to the point where the driving force for electron transfer alone is too small to move the $E°$ within the acceptable range for catalytic activity; that is, $E°$ is too low. However, by coupling a double protonation of the dapsox ligand to the Fe^{III} → Fe^{II} reduction, the Fe^{II} state of the complex is stabilized, as neutral H_2dapsox is a much weaker electron donor than $dapsox^{2-}$. This stabilization of the Fe^{II} state reduces the energy difference between the two oxidation states of the complex, raising $E°$ closer to an appropriate value for SOD activity. Additionally, the observation of low-energy MLCT transitions in the reduced complex suggests that the Fe^{II} ion is participating in backbonding with the ligand π^*-type orbitals, which will further stabilize the Fe^{II} state and thus provide additional driving force for the electron transfer. The combined effect of ligand protonation and π-backbonding is to tune the $E°$ of the complex such that it becomes catalytically active.

■ ASSOCIATED CONTENT

Ⓢ Supporting Information

Six figures and three tables showing room-temperature Abs spectra of aqueous solutions of $[Fe^{III}(dapsox)(H_2O)_2]ClO_4$ and $[Fe^{III}(dapsox)(H_2O)_2]NO_3$; low-temperature Abs and MCD spectra of both complexes; experimental and simulated EPR spectra of $[Fe^{III}(dapsox)(H_2O)_2]^+$; final computed energies of all spin states studied in the geometry-optimization calculations; Cartesian coordinates of DFT geometry-optimized models of the oxidized and reduced complexes; TD-DFT computational results for oxidized $[Fe^{III}(dapsox)(H_2O)_2]^+$; and INDO/S-CI computational results for reduced $[Fe^{II}(H_2dapsox)(H_2O)_2]^{2+}$. This material is available free of charge via the Internet at http://pubs.acs.org.

■ AUTHOR INFORMATION

Corresponding Author

*E-mail: brunold@chem.wisc.edu.

Notes

The authors declare no competing financial interest.

■ ACKNOWLEDGMENTS

T.C.B. thanks the NIH (GM 64631) for financial support and Dr. Frank Neese (MPI Mülheim) for providing ORCA free of charge. This research was supported in part by National Science Foundation Grant CHE-0840494

■ REFERENCES

(1) Miller, A.-F.; Sorkin, D. L. *Comments Mol. Cell. Biophys.* **1997**, *9*, 1−48.
(2) Fridovich, I. *J. Biol. Chem.* **1997**, *272*, 18515−18517.
(3) Choudhury, S. B.; Lee, J.-W.; Davidson, G.; Yim, Y.-I.; Bose, K.; Sharma, M. L.; Kang, S.-O.; Cabelli, D. E.; Maroney, M. J. *Biochemistry* **1999**, *38*, 3744−3752.
(4) Fridovich, I. *Acc. Chem. Res.* **1972**, *5*, 321−326.
(5) Bull, C.; Fee, J. A. *J. Am. Chem. Soc.* **1985**, *107*, 3295−3304.
(6) Bull, C.; Niederhoffer, E. C.; Yoshida, T.; Fee, J. A. *J. Am. Chem. Soc.* **1991**, *113*, 4069−4076.
(7) McAdam, M. E.; Levelle, F.; Fox, R. A.; Fielden, E. M. *Biochem. J.* **1977**, *165*, 81−87.
(8) Barrette, W. C.; Sawyer, D. T.; Fee, J. A.; Asada, K. *Biochemistry* **1983**, *22*, 624−627.
(9) Yost, F.; Fridovich, I. *J. Biol. Chem.* **1973**, *248*, 4905.
(10) Schininà, M. E.; Maffey, L.; Barra, D.; Bossa, F.; Puget, K.; Michelson, A. M. *FEBS Lett.* **1987**, *221*, 87−90.
(11) Stallings, W. C.; Pattridge, K. A.; Strong, R. K.; Ludwig, M. L. *J. Biol. Chem.* **1984**, *259*, 10695−10699.
(12) Lah, M. S.; Dixon, M. M.; Pattridge, K. A.; Stallings, W. C.; Fee, J. A.; Ludwig, M. L. *Biochemistry* **1995**, *34*, 1646−1660.
(13) Stallings, W. C.; Metzger, A. L.; Pattridge, K. A.; Fee, J. A.; Ludwig, M. L. *Free Radical Res. Commun.* **1991**, *12*−*3*, 259−268.
(14) Culotta, V. C.; Yang, M.; O'Halloran, T. V. *Biochim. Biophys. Acta* **2006**, *1763*, 747−758.
(15) Raha, S.; Robinson, B. H. *Trends Biochem. Sci.* **2000**, *25*, 502−508.
(16) Simonian, N. A.; Coyle, J. T. *Annu. Rev. Pharmacol. Toxicol.* **1996**, *36*, 83−106.
(17) Valentine, J. S.; Wertz, D. L.; Lyons, T. J.; Liou, L.-L.; Goto, J. J.; Gralla, E. B. *Curr. Opin. Chem. Biol.* **1998**, *2*, 253−262.
(18) Andjelkovíc, K.; Bacchi, A.; Pelizzi, G.; Jeremíc, D.; Ivanovíc-Burmazovíc, I. *J. Coord. Chem.* **2002**, *55*, 1385−1392.
(19) Liu, G.-F.; Filipovíc, M.; Heinemann, F. W.; Ivanovíc-Burmazovíc, I. *Inorg. Chem.* **2007**, *46*, 8825−35.
(20) Stoll, S.; Schweiger, A. *J. Magn. Reson.* **2006**, *178*, 42−55.
(21) Baerends, E. J.; Ellis, D. E.; Ros, P. *Chem. Phys.* **1973**, *2*, 41−51.

(22) Fonseca Guerra, C.; Snijders, J. G.; te Velde, G.; Baerends, E. J. *Theor. Chim. Acta* **1998**, *99*, 391−403.
(23) te Velde, G.; Baerends, E. J. *J. Comput. Phys.* **1992**, *99*, 84−98.
(24) Versluis, L.; Ziegler, T. *J. Chem. Phys.* **1988**, *88*, 322.
(25) Vosko, S. H.; Wilk, L.; Nusair, M. *Can. J. Phys.* **1980**, *58*, 1200−1211.
(26) Becke, A. D. *J. Chem. Phys.* **1993**, *98*, 5648.
(27) Perdew, J. P. *Phys. Rev. B* **1986**, *33*, 8822.
(28) Neese, F. ORCA 2.8.0, An Ab Initio, DFT and Semiempirical electronic structure package, 2009.
(29) Becke, A. D. *J. Chem. Phys.* **1993**, *98*, 1372.
(30) Lee, C.; Yang, W.; Parr, R. G. *Phys. Rev. B* **1988**, *37*, 785.
(31) Schaer, A.; Horn, H.; Ahlrichs, R. *J. Chem. Phys.* **1992**, *97*, 2571.
(32) Weigend, F.; Häser, M. *Theor. Chim. Acta* **1997**, *97*, 331−340.
(33) Schaer, A.; Huber, C.; Ahlrichs, R. *J. Chem. Phys.* **1994**, *100*, 5829.
(34) The PyMOL Molecular Graphics System, L., Version 1.5.0.1, Schrodinger.
(35) Neese, F. ORCA 2.9.1, An Ab Initio, DFT and Semiempirical electronic structure package. 2012.
(36) The ORCA basis set CoreProp was used. This basis is based on the TurboMole DZ basis developed by Ahlrichs and co-workers and obtained from the basis set library under ftp.chemie.unikarlsruhe.de/pub/basen.
(37) The Ahlrichs (2d2fg,3p2df) polarization functions were obtained from the TurboMole basis set library under ftp.chemie.unikarlsruhe.de/pub/basen. Sc-Zn: 2p functions were from Wachters, A. J. H. *J. Chem. Phys.* **1970**, *52*, 1033 plus one f-function from the TurboMole library.
(38) Kutzelnigg,W.; Fleischer, U.; Schindler, M. The IGLO method: Ab initio calculation and interpretation of NMR chemical shifts and magnetic susceptibilities. In *NMR: Basic Principles and Progress*, Vol. *23*; Diehl, P., Fluck, E., Günther, H., Kodfeld, R., Seelig, J., Eds.; Springer-Verlag: Heidelberg. Germany, 1990.
(39) Neese, F. *J. Chem. Phys.* **2001**, *115*, 11080−11096.
(40) Neese, F. *J. Chem. Phys.* **2005**, *122*, No. 034107.
(41) Hirata, S.; Head-Gordon, M. *Chem. Phys. Lett.* **1999**, *314*, 291−299.
(42) Hirata, S.; Head-Gordon, M. *Chem. Phys. Lett.* **1999**, *302*, 375−382.
(43) Ridley, J.; Zerner, M. *Theor. Chim. Acta* **1973**, *32*, 111−134.
(44) Zerner, M. C.; Loew, G. H.; Kirchner, R. F.; Mueller-Westerhoff, U. T. *J. Am. Chem. Soc.* **1980**, *102*, 589−599.
(45) Bacon, A. D.; Zerner, M. C. *Theor. Chim. Acta* **1979**, *53*, 21−54.
(46) Sarauli, D.; Meier, R.; Liu, G.-F.; Ivanovíc-Burmazovíc, I.; van Eldik, R. *Inorg. Chem.* **2005**, *44*, 7624−7633.
(47) Li, J.; Noodleman, L.; Case, D. A. Electronic structure calculations; Density functional methods with applications to transition metal complexes. In *Inorganic Electronic Structure and Spectroscopy*; Solomon, E. I., Lever, A., Eds.; John Wiley & Sons, Ltd: New York, 1999; Vol. *1*, p 669.
(48) Neese, F. *J. Biol. Inorg. Chem.* **2006**, *11*, 702−711.
(49) Solomon, E. I.; Pavel, E. G.; Loeb, K. E.; Campochiaro, C. *Coord. Chem. Rev.* **1995**, *144*, 369−460.
(50) Whittemore, D. O.; Langmuir, D. *J. Chem. Eng. Data* **1972**, *17*, 288−290.
(51) Grove, L. E.; Xie, J.; Yikilmaz, E.; Miller, A.-F.; Brunold, T. C. *Inorg. Chem.* **2008**, *47*, 3978−3992.
(52) Yikilmaz, E.; Porta, J.; Grove, L. E.; Vahedi-Faridi, A.; Bronshteyn, Y.; Brunold, T. C.; Borgstahl, G. E. O.; Miller, A.-F. *J. Am. Chem. Soc.* **2007**, *129*, 9927−9940.